IOP Publishing | Institute of Physics and Engineering in Medicine Physics in Medicine & Biology

Phys. Med. Biol. **60** (2015) 4797–4811 doi:10.1088/0031-9155/60/12/4797

Fetal magnetocardiography measurements with an array of microfabricated optically pumped magnetometers

Orang Alem[1,2], Tilmann H Sander[3], Rahul Mhaskar[1,2], John LeBlanc[4], Hari Eswaran[5], Uwe Steinhoff[3], Yoshio Okada[6], John Kitching[1], Lutz Trahms[3] and Svenja Knappe[1,2]

[1] National Institute of Standards and Technology, 325 Broadway, Boulder, CO 80305, USA
[2] University of Colorado, Boulder, CO 80309, USA
[3] Physikalisch-Technische Bundesanstalt, 10587 Berlin, Germany
[4] Charles S Draper Laboratories, 555 Technology Square, Cambridge, MA 02139, USA
[5] University of Arkansas for Medical Sciences, Little Rock, AR 72205, USA
[6] Boston Children's Hospital, Boston, MA 02115, USA

E-mail: tilmann.sander-thoemmes@ptb.de

Received 25 September 2014, revised 18 March 2015
Accepted for publication 7 April 2015
Published 3 June 2015

Abstract

Following the rapid progress in the development of optically pumped magnetometer (OPM) technology for the measurement of magnetic fields in the femtotesla range, a successful assembly of individual sensors into an array of nearly identical sensors is within reach. Here, 25 microfabricated OPMs with footprints of 1 cm^3 were assembled into a conformal array. The individual sensors were inserted into three flexible belt-shaped holders and connected to their respective light sources and electronics, which reside outside a magnetically shielded room, through long optical and electrical cables. With this setup the fetal magnetocardiogram of a pregnant woman was measured by placing two sensor belts over her abdomen and one belt over her chest.

The fetal magnetocardiogram recorded over the abdomen is usually dominated by contributions from the maternal magnetocardiogram, since the maternal heart generates a much stronger signal than the fetal heart. Therefore, signal processing methods have to be applied to obtain the pure fetal magnetocardiogram: orthogonal projection and independent component analysis. The resulting spatial distributions of fetal cardiac activity are in good agreement with each other. In a further exemplary step, the fetal heart rate was extracted from the fetal magnetocardiogram. Its variability suggests fetal activity.

We conclude that microfabricated optically pumped magnetometers operating at room temperature are capable of complementing or in the future even replacing superconducting sensors for fetal magnetocardiography measurements.

Keywords: atomic magnetometer, biomagnetism, fetal magnetocardiography, orthogonal projection, independent component analysis, microfabricated

(Some figures may appear in colour only in the online journal)

Introduction

Monitoring fetal heart signals during pregnancy is clinically important; for example, for the detection of fetal cardiac arrhythmia (Strasburger and Wakai 2010). Fetal heart signals have been recorded electrically for about 40 years. Fetal electrocardiography (fECG) has a good potential for obtaining additional information beyond echocardiography (Sameni and Clifford 2010). It can be recorded invasively with fetal scalp electrodes or non-invasively with electrodes on the maternal abdomen. Noninvasively monitored signals are generally of poor quality because the electrical potentials, conducted from the fetal heart to the maternal abdomen, are attenuated by the insulating waxy layer around the skin called vernix caseosa, which protects the skin of the fetus from the aqueous environment of the womb. The vernix caseosa is present from gestational age (GA) of approximately 27–36 weeks (Oostendorp *et al* 1989a,b, Pieri *et al* 2001, Quinn *et al* 1994). In contrast to electrical potentials, magnetic fields are not heavily distorted by this thin insulating layer (Kariniemi *et al* 1974, Wakai *et al* 2000). Therefore, biomagnetic approaches have a distinct advantage over the electrical counterparts (Sameni and Clifford 2010), but fetal magnetocardiography (fMCG) systems are more complicated and expensive.

Currently, biomagnetic signals such as fetal magnetocardiogram (fMCG) and magnetocardiogram (MCG) of adults are recorded with superconducting quantum interference devices (SQUIDs) (Grimm *et al* 2003, Fenici *et al* 2005). MCG instruments based on SQUIDs have been very useful in noninvasively detecting fMCG signals (Strasburger *et al* 2008, Van Leeuwen *et al* 2014). However, the sensors in such an MCG system are fixed in shape within a large cryostat called a Dewar. The fixed shape has limited the flexibility in placing the sensors optimally around the abdomen of a pregnant mother as the size and shape of the maternal abdomen undergoes dramatic changes during the pregnancy. Thus, there are advantages of a system with a flexible array of sensors that can fit conformally over the abdomen throughout all GAs of the fetus. The flexible placement also allows for easy recording of the mother's MCG (mMCG), which is always superimposed on the fMCG as an unwanted signal component and has to be distinguished from the fetal heart signals by offline data processing.

We report the development of an array of small uncooled sensors that provides the flexibility required for optimal measurements of fMCG. Magnetic fields sensors based on the spectroscopy of alkali atoms and operating at room temperature have been steadily progressing over the last decade. Pioneering work in the recording of MCG with optically pumped magnetometers (OPMs, OPM is synonymous with atomic magnetometer) used one or two vapor cells with dimensions of 20 mm or larger (Livanov *et al* 1981, Bison *et al* 2003, Belfi *et al* 2007, Kim *et al* 2007, Kamada *et al* 2012) and systems have progressed to static arrays of several tens of sensors (Bison *et al* 2009, Lembke *et al* 2014). There has been only one fMCG demonstration to date with a small static array of four OPMs (Wyllie *et al* 2012). Smaller

OPMs, which can be placed in variable geometries have also been used for MCG (Knappe *et al* 2010, Shah and Wakai 2013) and are particularly suitable for flexible multichannel fMCG arrays, since the curvature of the abdomen during pregnancy is difficult to cover with large sensors or static sensor arrays. Microfabricated OPMs (μOPMs) with footprints of less than 1 cm^2 (Mhaskar *et al* 2012), allow for highly conformal designs of large and densely arranged arrays. Single sensor magnetoencephalography (MEG) has been demonstrated with similar sensors (Sander *et al* 2012, Knappe *et al* 2014).

We developed a flexible 25-channel system of μOPMs and evaluated this system on a fetus at GA of 32 weeks as a technical study. Due to fetal movement we do not know the precise location of the fetus' heart. To demonstrate the geometrical capabilities of the design, the sensors were placed not only conformal in proximity to the fetus on the mother's abdomen, but also placed deliberately over the mother's chest. This combination allows for the simultaneous recording of both the fMCG and mMCG. As fMCG reported in the literature is derived from raw data using signal processing we extended the hardware results in a similar way. Besides calculating averaged MCGs we applied typical statistical multivariate methods to separate fMCG from mMCG. Two independent methods were compared: orthogonal-projection (OP) algorithms (Mccubbin *et al* 2006) and independent-component analysis (ICA) (Comani *et al* 2004). Since a detailed fetal heart rate (FHR) is clinically of interest, we demonstrated its extraction from data processed using OP.

Materials and methods

Miniature atomic magnetometers and array design

The multichannel μOPM array consisted of 25 microfabricated sensor heads (Mhaskar *et al* 2012) connected to a common control unit by optical fibers of 5 m in length. A photograph of a sensor head with fibers, a photograph of the thermal insulation platform, and an operational schematic are shown in figures 1(a)–(c). The sensor heads were inserted into 3 D printed receptacles mounted on three flexible belts (see figure 3). Each pair of neighboring sensors is fixed parallel to each other at a separation of 4 cm; however, the relative position of adjacent sets could vary as the belts bend to follow the contour of the abdomen.

Each sensor head contains a microfabricated ^{87}Rb vapor cell (Liew *et al* 2004), with inner volume of $(1.5\,mm)^3$, suspended inside a vacuum enclosure. The atoms in the cell are spin-polarized with light from a diode laser at 795 nm, transmitted to the sensor head via a polarization-maintaining optical fiber. The light is circularly polarized on the sensor head with a quarter-wave plate and polarizes the atoms along the direction of the laser beam. In the presence of a magnetic field component perpendicular to the axis of polarization, the orientation of the atomic spins changes, resulting in a change of the transmitted light intensity. Phase-sensitive detection was implemented by applying a small, modulating magnetic field perpendicular to the laser beam and detecting the resulting modulation of the transmitted light with a photodiode. The Helmholtz coils used for field modulation of each individual sensor are part of an additional sensor housing (housing not shown in figure 1), which fits into the belts in figure 3. The Helmholtz coils sketched in figure 1 generate a field perpendicular to the belt surface, allowing the sensors to measure the field component normal to the surface of the abdomen. All sensors were inserted with the same orientation.

For these sensors, the change in the transmitted power of the pump beam is proportional to the projected magnitude of the external field in the direction of the modulation field (Dupont-Roc *et al* 1969). To achieve an Rb vapor density that optimizes the magnetometer performance, a second light beam from a laser at 1480 nm is coupled into the sensor probe, collinear with the

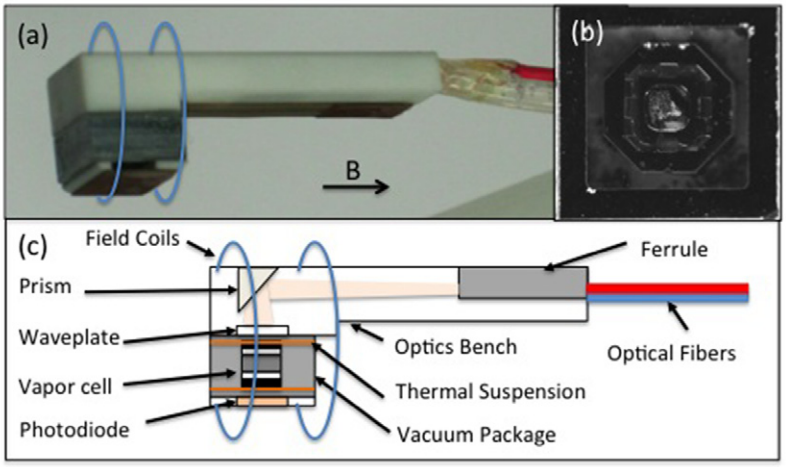

Figure 1. (a) Photograph of a microfabricated sensor head, with the optical fibers on the right and the vacuum package containing the vapor cell on the left. A photodiode mounted onto a flexible circuit sits underneath the vapor cell. The black arrow in the photograph indicated the direction of the magnetic field component measured, the field coils are sketched in blue. (b) Photograph of the vacuum package. The cell can be seen in the center held by the thermal suspension, which is mounted to a support of octagonal shape. (c) A pump/probe laser is circularly polarized by a $\lambda/4$ plate, then passes through the atomic-vapor cell and is detected by the photodiode. A second laser is used to heat the vapor cell to ~150 °C through the absorption of the light power by the colored glass filters. A set of Helmholtz coils apply a modulation field for phase-sensitive lock-in detection.

pump light, and absorbed by the filters on the cell windows, which heats the cell to a temperature of 150 °C. The vapor cell is thermally isolated inside the sensor head using a polyimide suspension system and vacuum packaging (Mescher *et al* 2005) as shown in figure 1(b)). The 150 °C vapor cell can be places less than 5 mm from the subject's skin with no ill thermal effects.

The sensitivity of the sensors can be assessed from figure 2, which shows the noise spectra of sensors measured in a tabletop magnetic shield. The recording bandwidth for the spectra was 500 Hz and the increase above 100 Hz is the bandwidth imposed by the atoms. Orange curves correspond to sensors, whose data were rejected during the measurements taken in BMSR II. Their peak-to-peak noise exceeded 120 pT. The white noise level of all sensors was increased by a factor of 2–5 during the measurements in BMSR II. While we do not know the cause of the noise increase, it seemed to appear especially at frequencies below 10 Hz in the rejected sensors. One of the reasons for the noise increase could be excessive intensity noise of the laser and additional intensity and polarization noise due to movement or strain on the optical fibers (see section Measurement setup). Two sensors ceased to operate most likely due to a failure of the vacuum enclosure. This type of sensor is optimized for ambient magnetic fields below $\pm$10 nT due to the suppression of spin-exchange relaxation (Happer and Tang 1973, Allred *et al* 2002). The bandwidth, which is limited by the relaxation period of the atoms, is approximately 200 Hz.

OP and independent component analysis for magnetocardiography

The fMCG is measured in the presence of environmental noise and other biological magnetic interference such as mMCG, the biggest interference after removing environmental noise. To

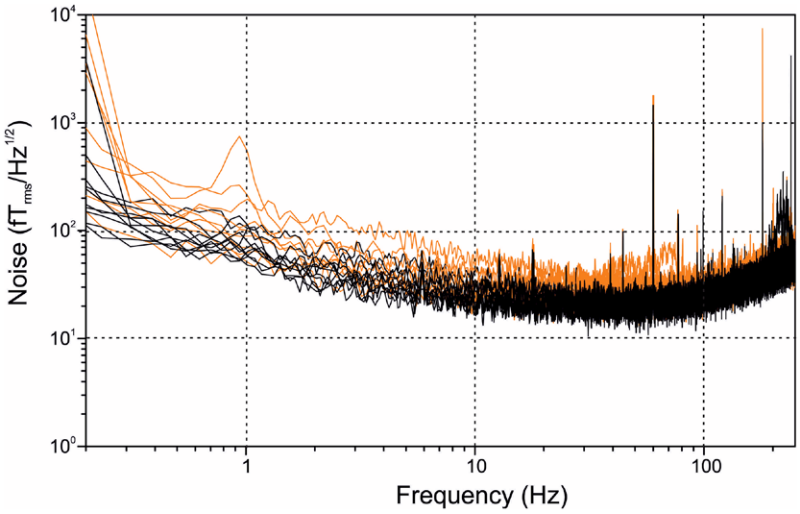

Figure 2. Noise equivalent magnetic field for 19 of the 25 manufactured sensors. A subset (10) of the 16 sensors used for further data analysis is shown in black and the discarded nine sensors are shown in orange.

produce a clean fMCG signal, it is essential to separate it from the mMCG signal. Here, we apply two well-established methods to separate fMCG and mMCG to evaluate to what extent they can be successfully applied to fMCG data taken with μOPMs. While we are aware that these methods have their limitations, we apply them without further validation. OP is one of the methods that is used to separate fMCG signals from mMCG (Lowery *et al* 2003) if a multichannel dataset is recorded. The unwanted interference is projected out of the measurement in the temporal domain by constructing the OP operator from signal-space vectors corresponding to the interfering components—in this case mMCG (Vrba *et al* 2004). OP starts with the selection of a template mMCG QRS complex. Each instant of the maternal QRS segment is determined. An ensemble average is performed and the resulting averaged cardiac cycle is used to determine the signal-space vectors corresponding to mMCG. These mMCG vectors are denoted by v_1, v_2, v_3,…,v_n, where n is the number of vectors, and are combined in a matrix $\mathbf{V}$ with dimensions $m \times n$, where m is the number of channels,

$$\mathbf{V} = (v_1, v_2, v_3, ..., v_n). \tag{1}$$

The vectors $\mathbf{V}$ are then projected out of the data by multiplying the measured multichannel signal $\boldsymbol{x}(t)$ with an operator $\mathbf{P}$ as

$$\boldsymbol{x}'(t) = (\mathbf{I} - \mathbf{V}(\mathbf{V}^{\mathrm{T}}\mathbf{V})^{-1}\mathbf{V}^{\mathrm{T}})\boldsymbol{x}(t) = \mathbf{P}\boldsymbol{x}(t), \tag{2}$$

where $\mathbf{I}$ is the identity matrix.

An alternative method to dissociate the superposition of fMCG and mMCG and other technical noise sources is independent component analysis (ICA). In contrast to OP it does not require to determine the R-peaks in the mMCG. The second-order blind-identification algorithm (SOBI, TDSEP is a synonymous abbreviation) (Belouchrani *et al* 1997, Ziehe and Müller 1998) uses time-delayed covariance matrices $\mathbf{C}_\tau$ of the form

$$\mathbf{C}_\tau = \left\langle x_i(t), x_j(t+\tau) \right\rangle_t, \tag{3}$$

where x_i (x_j) denotes the time series of the ith (jth) signal channel, with indices $i, j = 1\ldots m$ and m being the number of channels. These covariance matrices are calculated for a set of several delay values $\{\tau\}$ and the matrix operator $\mathbf{W}$, which simultaneously diagonalizes these matrices, is estimated. With this operator the measured data can be written as

$$\boldsymbol{x}(t) = \mathbf{W}\boldsymbol{s}(t), \tag{4}$$

where one $s_i(t)$ might represent the mMCG and another $s_{j\neq i}(t)$ might represent fMCG (Sander *et al* 2007). Real sources with multiple degrees of freedom can be represented by several source components $s_i(t)$. The SOBI decomposition of the μOPM data used a set of matrices $\{\mathbf{C}_\tau\}$ as defined in equation (3) with $\{\tau\} = 0.05, 0.1, 0.15, ..., 1000$ ms. These 20 000 matrices are mainly diagonal, but oscillating signals present in several channels and with a frequency of $1 / \tau_k$ lead to non-zero off diagonal elements in $\mathbf{C}_{\tau k}$. The largest $\tau_k = 1000$ ms corresponds to a frequency of 1 Hz and therefore signals down to 1 Hz can be extracted. This is reasonable for a superposition of maternal and fetal heart signals.

Measurement setup

The measurements were made within the BMSR II magnetically shielded room (MSR) at the Physikalisch Technische Bundesanstalt in Berlin, Germany (Bork *et al* 2001). The sensor fiber/wire bundles were fed through openings in the walls of BMSR II to reach the lasers and electronics outside of the shielded room. The sensor belts were fastened on the abdomen and chest of the mother as shown in figure 3. The distance between the center of the sensitive volume of the magnetometer and the skin was approximately 4.5 mm. In total, 25 sensor probes were mounted on the belts and used for measurement, but only data from 16 sensors were used for analysis as data from sensors with higher noise levels were rejected. We suspect that the large additional noise, which mainly occurred in the sensors on the edges of the belts was caused by sharp bending of the optical fibers, since 5 m fiber cable was only barely enough to span the distance between the electronics and the inside of the shielded room. The sensitivity had to be optimized once a day to compensate for changes in fiber coupling efficiency of one pump laser. These effects require further investigation. An automated optimization procedure is needed as well as adding stress relive to the sensor holder.

Several measurements with duration of 300 s and with slightly different belt placements were performed during a single day. Another measurement was performed on the second day and reproducibility was established. The results reported below used the sensor configuration depicted in figure 3.

The study was performed in accordance with the principles of the Declaration of Helsinki. The legal institutional human subject review scheme was applied. It restricts research to healthy volunteers including pregnant women and strictly non-invasive methods. Written consent from the volunteer was obtained.

Data preprocessing with software lock-in

For each sensor probe the output signal of the photodiode in figure 1 was amplified and digitized with a sampling rate of 20 kHz using a custom made 24-bit data acquisition system. The 20 kHz sampling frequency is sufficient for a proper sampling of the signal modulated at 1.7 kHz. This modulation frequency is optimal with respect to μOPM sensor sensitivity. The modulation coil signal was recorded in an additional channel and used as the reference signal in the software lock-in. The mathematical formulation of a lock-in can be found in (Scofield 1994) and it was realized in Matlab™ (www.mathworks.com).[7] Before multiplication with

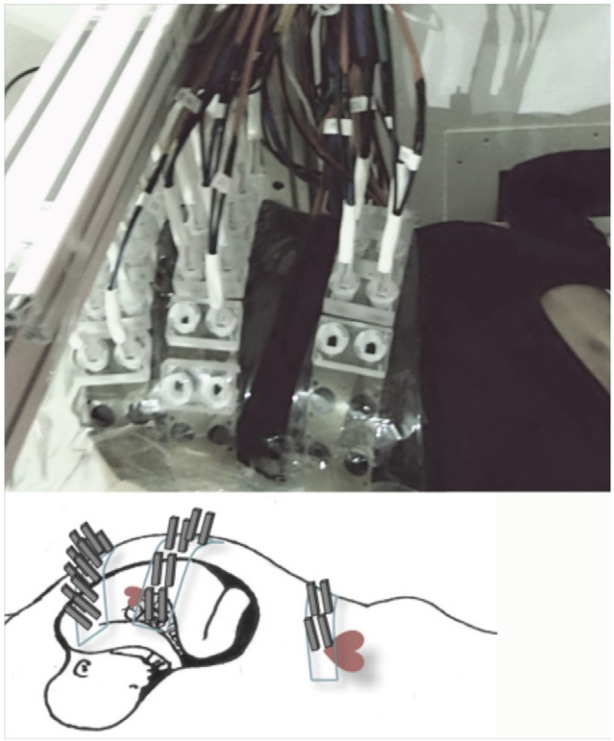

Figure 3. (Top) View of the three sensor belts attached to the abdomen and chest of a pregnant women lying on her back during the measurement. The sensor fiber and wire bundles are supported by an aluminum beam visible in the top left corner. The bundles leave the MSR through a hole and connect to the control electronics outside. Unused sensor receptacles are seen towards the front of the belts. (Bottom) The sketch shows the sensor probe placements in relation to the anatomy of the mother and fetus. The single belt on the right measures the mMCG while the two belts on the abdomen are placed in close proximity to the fetus.

the photodiode signal the reference signal was phase-shifted by 92° (odd value due to discrete time step). This phase shift was close to the optimum phase shift of 100° measured with a commercial digital lock-in amplifier running in parallel to a selected channel for control purposes. After the multiplication step a low-pass filter was applied with a corner frequency set at 40 Hz and a roll-off greater than 20 dB/octave. Finally the data were high-pass-filtered at 0.5 Hz and these data will be considered as the raw data in the following analysis. Data without high pass filtering do show maternal respiration related baseline shifts as expected.

Results

Fetal MCG extracted by OP

A time segment of 4 s from the recorded 300 s of raw multi-channel μOPM data is shown in figure 4. Channels with a noise levels greater than 120 pT (peak to peak) were excluded here

[7] Trade name is stated for technical clarity and does not imply endorsement by NIST. Products from other manufacturers may perform as well or better.

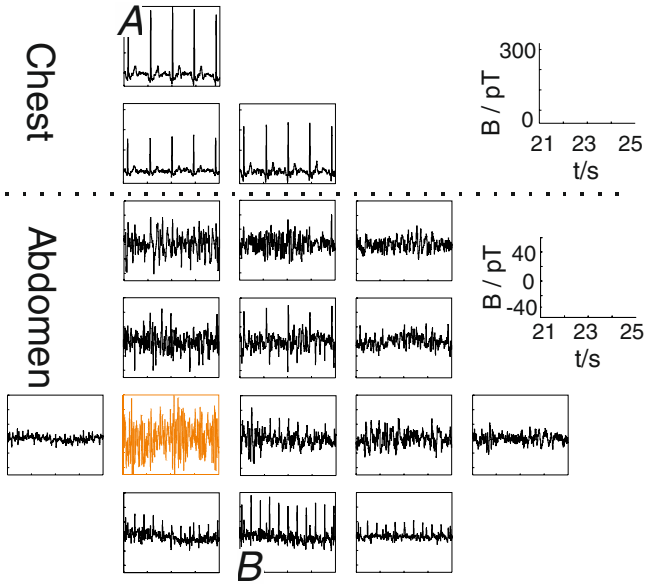

Figure 4. The raw multichannel data recorded with the μOPM array show the mMCG in the channels over the mother's chest, while sensors on the lower part of the abdomen show a rapid succession of peaks, typical for an fMCG. The dotted line indicates that the sensors over the chest and abdomen are separated by a gap; see the photo in figure 3 (top). The orange channel is an example of a rejected channel with higher noise levels. For clarity, the B field scale is chosen differently for the chest and abdominal channels as indicated. For channels marked *A* and *B* see the text.

and in further calculations. One example of a rejected channel is shown in orange. The noise spectrum of the rejected channel is included in the orange channels in figure 2, corresponding to those with higher noise levels. The mMCG in the chest channels shows a heart rate of approximately 60 beats per minute (bpm), while the measurements from the abdomen clearly indicate a more rapid peak sequence. These peaks correspond to the fMCG signals. P- and T-wave can be observed.

To extract the heart rate of the fetus reliably, it is necessary to remove the mMCG from the abdomen data using, e.g. the OP method as discussed in the 'Materials and Methods' section. Here a 2D operator $\boldsymbol{V}$ (see equation (1)) resulted. Figure 5 shows the data of channels marked *A* and *B* in figure 4, after OP. The fMCG is clearly visible in cannel B as the rapid heartbeat. A visual comparison of the results from channel *A* in figure 5 with the original data in figure 4 shows that the mMCG is suppressed by the OP as intended. Note that channel *A* in figure 5 is plotted with the fine scaling of 40 pT and not the 300 pT scaling of figure 4.

A difference in noise (sensitivity) between the individual sensors is visible in the channels over the abdomen. The sensitivity range of the μOPMs is similar to the performance of earlier multichannel SQUID systems; nevertheless, a more homogeneous set of sensors would be desirable. An estimate for the signal-to-noise ratio (SNR) of the fMCG recorded with the μOPM can be made from channel *B* in figure 5. A peak-to-peak noise of 10 pT and a fetal R-peak height of 40 pT are observed corresponding to an SNR of 4. This is close to a typical SNR of 10 for SQUID recordings, which can be estimated from data shown in (Sander *et al* 2007) with peak-to-peak noise of 100 fT and fetal R-peak heights around 1 pT.

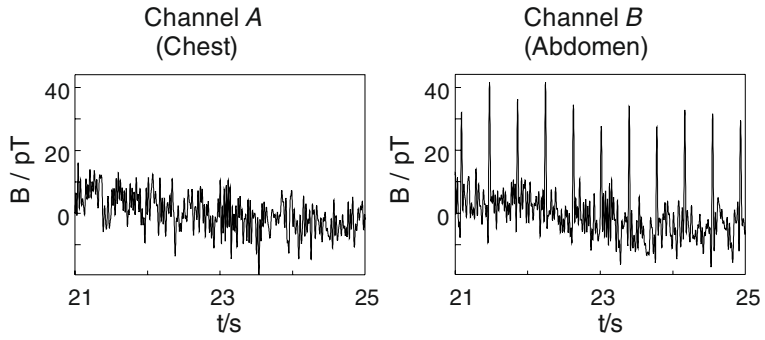

Figure 5. The success of mMCG suppression by OP is evident by comparing channels marked *A* and *B* in figure 4 with the same channels shown here after projection out the mMCG. The mMCG R-peaks in channel *A*, visible in figure 4, are absent here. Eleven fMCG R-peaks in channel *B* are clearly visible in the 4 s section displayed, indicating a FHR of more than 150 bpm.

Of great diagnostic potential is the estimation of the FHR. Robust methods to determine QRS complexes were developed in (Steinhoff *et al* 2005) and (Wilson *et al* 2008). The FHR shown in figure 6 was determined from the QRS-Hilbert method (Wilson *et al* 2008) applied to the fMCG. Strong variations of the FHR occur in the 300 s recording. In general, these large variations in FHR could be related to the fetus being in an active state.

For signal analysis methods such as averaging of heart beat patterns or statistical methods such as ICA the input data should ideally be stationary. Therefore, a 30 s window with a fairly constant heart rate is chosen from figure 6 and the fMCG from this window is used in the following spatial analysis.

Spatial analysis by averaging and ICA

To increase the SNR of an MCG, an average beat can be calculated by determining the R-peak and averaging individual beats that are aligned with respect to the R-peak position. The R-peak positions of the mMCG were detected by thresholding the signal of the topmost channel in figure 4. The fMCG R-peak positions were determined before for the FHR estimation. A 30 s interval of data, indicated in figure 6, was selected for the average (baseline interval: time window between P-wave and QRS complex). It contained approximately 30 beats for the mMCG and 75 beats for the fMCG. The mMCG average was calculated from raw data, the fMCG average from the data after OP processing. The averaged heart cycles are shown in figure 7 together with the respective R-peak map and a single unaveraged heart beat. The fetal P-wave is visible only in the average and a T-wave is not visible. Ideally, these features of the fMCG should be visible in the raw data for best clinical benefit. But depending on GA these features have not been detected in averaged fMCGs recorded with SQUIDs either (van Leeuwen *et al* 2004). Therefore, the absence of the T-wave here is not necessarily due to the lower SNR of the μOPMs compared to SQUIDs.

It can be seen from the R-peak mMCG map (figure 7(a)) that the mMCG clearly extends into the abdominal channels. The gap between the channels over the chest and abdomen is marked in maps by a dotted line. The R-peak map of the fMCG (figure 7(b)) shows a dipolar pattern in the abdominal channels only. The separation of the extrema in the dipolar R-peak map is approximately 10–12 cm (as estimated based on the photo in figure 3 and the known 4 cm distance between neighboring sensors). This indicates a source located in the abdomen

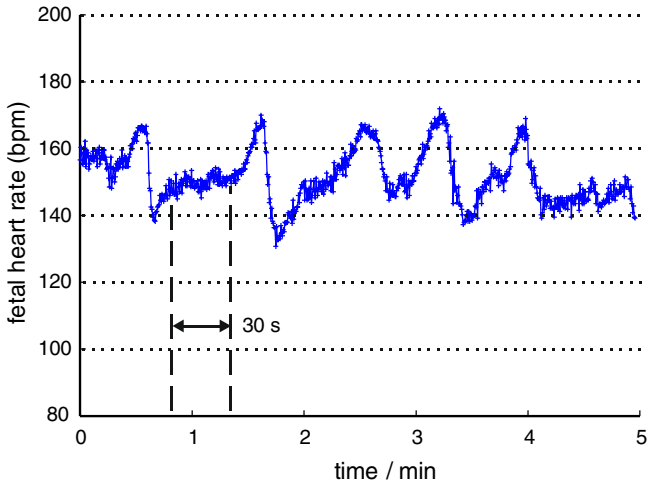

Figure 6. The FHR extracted from the fMCG is quite variable and sudden changes could indicate the fetus being in an active state. The R-peaks were determined using the robust procedure described in Wilson *et al* (2008) after removing the mMCG using OP. The marked 30 s window with a fairly constant heart rate is chosen for further calculations.

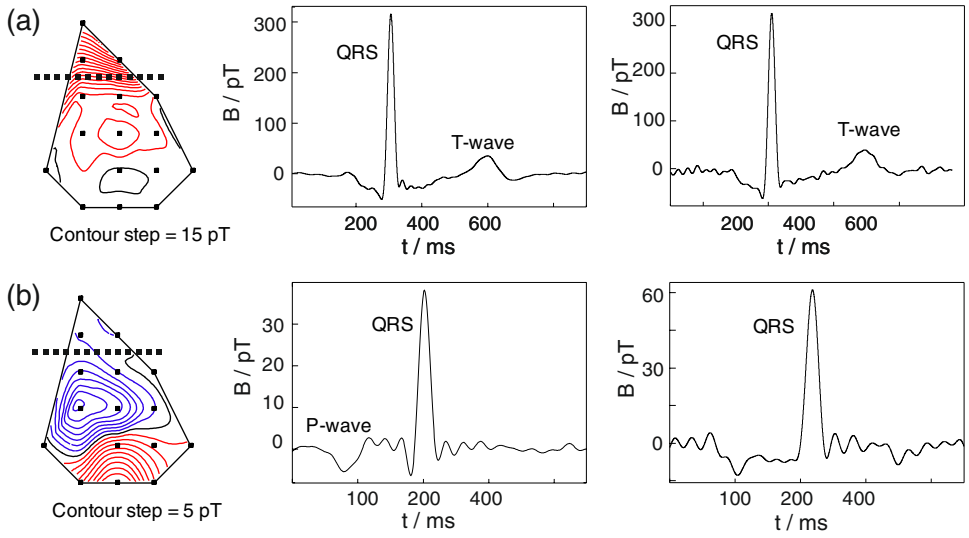

Figure 7. (a) Average R-peak mMCG map (left), averaged mMCG cycle (middle), and raw mMCG cycle (right); (b) Average R-peak fMCG map (left), averaged fMCG cycle (middle), raw fMCG cycle (right). The channels shown correspond to channels marked *A* and *B* in figure 4. The mMCG T-wave is visible in the raw data; a clear fMCG P-wave is visible only in the average. Note: the blue and red colors indicate negative and positive values of the magnetic field, respectively.

as it is expected for fetal heart activity. Due to volume conducting effects in the abdomen, the depth of the sources cannot be estimated easily.

To separate the fMCG from the mMCG the SOBI ICA, as discussed in the 'Materials and Methods' section was applied to the presumably stationary data in the 30 s interval highlighted

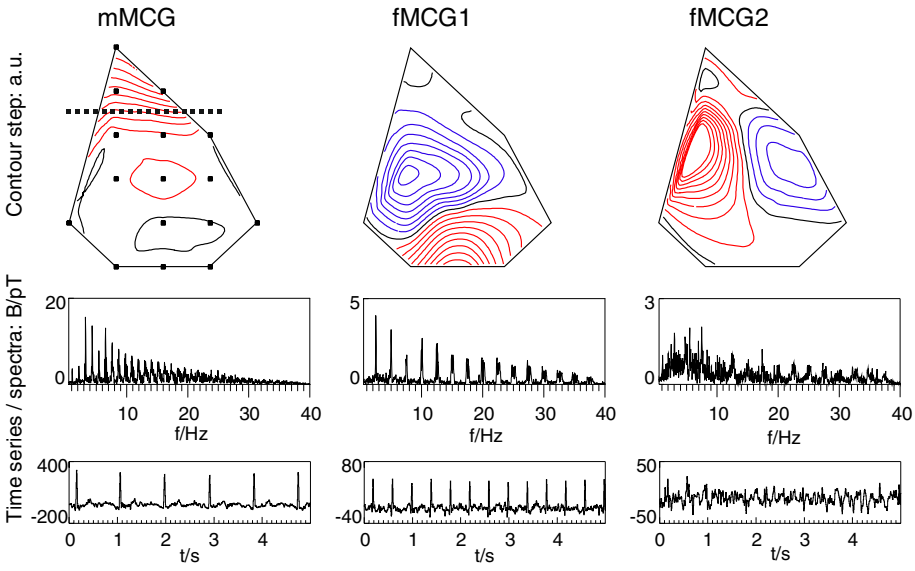

Figure 8. Three ICA components attributed to mMCG and fMCG are shown as maps (top), power spectra of the time series (middle), and time series (bottom, only 5 s displayed). The mMCG component is dominant over the upper section of the map, corresponding to the chest measurements (markers and dotted line in map as in figure 7). The time series and its spectrum indicate a maternal heart rate of 60 bpm. The fMCG1 component shows a dipolar map over the abdomen similar to the R-peak map in figure 7(b) (for fMCG2 see text).

in figure 6. The ICA yields as many components as there are channels, requiring a manual selection of components by secondary information. Only three components had time series or spectra related to the known maternal and FHRs. The spatial distributions of these components are shown in figure 8 along with their associated time series and power spectra (see equation (4): Maps are the columns of **W**). The left component represents the mMCG because the pattern is very similar to the average mMCG in figure 7(a). The corresponding spectrum shows the maternal heart rate. The fMCG1 component (middle) corresponds well to the averaged fMCG map at the R-peak position in figure 7(b). The fMCG1 spectrum indicates a heart rate of 150 bpm consistent with figure 6. The fMCG2 component (right) was selected as it has a dipolar pattern over the upper abdomen and might be related to the fMCG. Using ICA allowed extracting the fMCG without the need to search for the fetal R-peaks.

Discussion

The recording of fMCGs with OPMs can draw on the analysis techniques developed for fMCG data obtained with SQUID sensors. The first step is often to separate fetal MCG signals from interfering biological noise, such as maternal MCG. We have applied two different methods, OP and ICA, to effectively extract the fetal cardiac signals from the mixture of biological signals as well as environmental noise. The overall consistency of the results from both methods is an indicator for the quality of the raw data. Subsequent to fMCG extraction often the aim is to estimate fetal R–R intervals for the purpose of general heart rate variability (HRV) analysis and during the antepartum period. Our results indicate that fetal R–R intervals can be determined easily from fMCG data recorded with OPMs.

In order to fully utilize the potential of the μOPM array, we should take advantage of the conformal and geometric flexibility through the ability of conveniently placing arrays of sensors in desirable locations on the abdomen and the chest. The possibility to extend the sensor coverage over the thorax resulted in clear ICA field maps for both mMCG and fMCG. Our ICA results are consistent with maps obtained by averaging the QRS complexes. The extraction of the fMCG in the abdominal channels with the OP method was very efficient suggesting that the characterization of the mMCG through recording channels over the chest is beneficial, although a quantitative analysis of the effect is left to future work. Such a benefit cannot be achieved by recording a maternal ECG, since the potential distribution measured by ECG is not easily transferable to a magnetic field maps. The large area of coverage might be particularly beneficial in combination with a method proposed by (Vullings and Mischi 2013), which uses an electrical source model of the mother's heart in combination with a multivariate statistical method to extract the fMCG.

The importance of the multichannel sensor layout, as realized here, is stressed in (Van Leeuwen *et al* 2004), which finds differences in fetal cardiac time interval results between data from two fixed-geometry SQUID sensor arrays used in the study. Further, in Gustafson *et al* 2011 a consistent pattern related to diaphragmatic movements *in utero* is isolated from fMCGs using ICA. These movements are the precursors to respiration. Respiration can influence HRV, which is an important diagnostic marker in adults. Using the multichannel μOPM array, the fetal HRV results of (Gustafson *et al* 2011) might be tested on a much larger sample of pregnant women. The identification of the diaphragmatic movements might be simplified using the multichannel μOPM sensor due to an increased spatial coverage of the womb.

The experiments presented here were conducted in the highly magnetically shielded room BMSR II. The BMSR II consists of seven layers of μ-metal shielding. It has remnant fields below 1 nT and a shielding factor of 10 000 at 0.1 Hz. These properties allow the μOPMs to operate within their optimal dynamic range. Nevertheless, optically pumped magnetometers operating under similar conditions have previously been validated in standard two-layer MSRs for measurements of MEG (Johnson *et al* 2013, Shah and Wakai 2013) and fetal MCG (Wyllie *et al* 2012), as well as MEG in human size shield cans (Xia *et al* 2006). As two-layer MSRs have a shielding factor of only 100 at 0.1 Hz, operating our sensors in such a MSR will require either use one of the sensors to lock a common background field (Wyllie *et al* 2012) or to use the coils already present on the individual sensor heads to operate under negative feedback (Shah and Wakai 2013, Lee *et al* 2014). While these previous experiments have successfully demonstrated the feasibility, our measurements should be repeated in standard two-layer MSRs and also human size shield cans in the future.

Conclusions

Here, we demonstrated that μOPMs are an attractive alternative to SQUID sensors for the measurement of fMCG; they operate without a cryogenic infrastructure, facilitate closer proximity placement to the signal sources, and allow for variable and conformal sensor array geometries. Well-tested algorithms yielded convincing FHRs and fetal field maps from the data presented here. It suggests that the μOPM data quality can be similar to that of SQUIDs for this type of application. Numerically, the SNR found here was comparable for SQUIDs and μOPMs due to the reduced distance between the fetal heart and the sensor. All fetal heart measurements, typically explored by SQUID systems, are potentially accessible using the non-cryogenic multichannel μOPM sensor technology, which still requires a costly MSR.

We believe that this paper presents the first publication of biomagnetic measurements with a larger conformal array of optically pumped magnetometers. While we present a

proof-of-principle experiment to evaluate the possibility of its use for fetal assessments, there is much technical development needed. In our experiments, 9 out of 25 sensors showed large field fluctuations, which we believe, were largely caused by strains on the optical fiber connections during movement of the array. Furthermore, further development of the control system to ensure optimal performance over long times is needed. Finally, it needs to be shown that the sensors can be operated under negative feedback to linearize the performance and extend the dynamic range and that simple gradiometric operation is sufficient to operate these sensors inside standard magnetically shielded rooms. Implementing these methods in a larger conformal array will be necessary in the future.

Acknowledgments

Technical support by W Müller with the data acquisition system was very helpful. We thank P van Leeuwen for helpful discussions.

This work is a contribution of NIST, an agency of the US Government, and is not subject to copyright.

References

Allred J C, Lyman R N, Kornack T W and Romalis M V 2002 High-sensitivity atomic magnetometer unaffected by spin-exchange relaxation *Phys. Rev. Lett.* **89** 130801

Belfi J, Bevilacqua G, Biancalana V, Cartaleva S, Dancheva Y and Moi L 2007 Cesium coherent population trapping magnetometer for cardiosignal detection in an unshielded environment *J. Opt. Soc. Am.* B **24** 2357–62

Belouchrani A, Abed-Meraim K, Cardoso J F and Moulines E 1997 A blind source separation technique using second-order statistics *IEEE Trans. Sig. Process.* **45** 434–44

Bison G, Castagna N, Hofer A, Knowles P, Schenker J L, Kasprzak M, Saudan H and Weis A 2009 A room temperature 19-channel magnetic field mapping device for cardiac signals *Appl. Phys. Lett.* **95** 173701–3

Bison G, Wynands R and Weis A 2003 A laser-pumped magnetometer for the mapping of human cardiomagnetic fields *Appl. Phys.* B **76** 325–8

Bork J, Hahlbohm H D, Klein R and Schnabel A 2001 The 8-layered magnetically shielded room of the PTB: design and construction *Proc. 12th Int. Conf. on Biomagnetism* ed J Nenonen *et al* (Espoo: Helsinki University of Technology) pp 970–3

Comani S, Mantini D, Alleva G, Di Luzio S and Romani G L 2004 Fetal magnetocardiographic mapping using independent component analysis *Physiol. Meas.* **25** 1459–72

Dupont-Roc J, Haroche S and Cohen-Tannoudji C 1969 Detection of very weak magnetic fields (10–9 gauss) by Rb zero-field level crossing resonances *Phys. Lett.* A **28** 628–39

Fenici R, Brisinda D and Meloni A M 2005 Clinical application of magnetocardiography *Expert Rev. Mol. Diagnostics* **5** 291–313

Grimm B, Haueisen J, Huotilainen M, Lange S, Van Leeuwen P, Menendez T, Peters M J, Schleussner E and Schneider U 2003 Recommended standards for fetal magnetocardiography *Pacing Clin. Electrophysiol.* **26** 2121–6

Gustafson K M, Allen J J, Yeh H W and May L E 2011 Characterization of the fetal diaphragmatic magnetomyogram and the effect of breathing movements on cardiac metrics of rate and variability *Early Hum. Development* **87** 467–75

Hansman C F 1966 Growth of interorbital distance and skull thickness as observed in roentgenographic measurements *Radiology* **86** 87–96

Happer W and Tang H 1973 Spin-exchange shift and narrowing of magnetic resonance lines in optically pumped alkali vapors *Phys. Rev. Lett.* **31** 273

Johnson C, Schwindt P D D and Weisend M 2013 Multi-sensor magnetoencephalography with atomic magnetometers *Phys. Med. Biol.* **58** 6065–77

Kamada K, Ito Y and Kobayashi T 2012 Human MCG measurements with a high-sensitivity potassium atomic magnetometer *Physiol. Meas.* **33** 1063–71

Kariniemi V, Ahopelto J, Karp P J and Katila T E 1974 The fetal magnetocardiogram *J. Perinat. Med.* **2** 214–6

Kim K, Won-Kyu L, Kim I, X, Seon and Han Seb M 2007 Atomic vector gradiometer system using cesium vapor cells for magnetocardiography: perspective on practical application *IEEE Trans. Instrum. Meas.* **56** 458–62

Knappe S, Sander T H, Kosch O, Wiekhorst F, Kitching J and Trahms L 2010 Cross-validation of microfabricated atomic magnetometers with superconducting quantum interference devices for biomagnetic applications *Appl. Phys. Lett.* **97** 133703

Knappe S, Trahms L and Sander T 2014 Optically-pumped magnetometers for MEG *Magnetoencephalography: From Signals to Dynamic Cortical Networks* ed S Supek and C J Aine (Berlin: Springer)

Lee H J, Shim J H, Moon H S and Kim K 2014 Flat-response spin-exchange relaxation free atomic magnetometer under negative feedback *Opt. Express* **22** 19887–94

Lembke G, Erné S N, Nowak H, Menhorn B and Pasquarelli A 2014 Optical multichannel room temperature magnetic field imaging system for clinical application *Biomed. Opt. Express* **5** 876–81

Liew L A, Knappe S, Moreland J, Robinson H, Hollberg L and Kitching J 2004 Microfabricated alkali atom vapor cells *Appl. Phys. Lett.* **84** 2694–6

Livanov M N, Kozlov A N, Sinelnikova S E, Kholodov J A, Markin V P, Gorbach A M and Korinewsky A V 1981 Record of the human magnetocardiogram by the quantum gradiometer with optical pumping *Adv. Cardiol.* **28** 78–80

Lowery C L, Campbell J Q, Wilson J D, Murphy P, Preissl H, Malak S F and Eswaran H 2003 Noninvasive antepartum recording of fetal S-T segment with a newly developed 151-channel magnetic sensor system *Am. J. Obstet. Gynecol.* **188** 1491–6

Mccubbin J, Robinson S E, Cropp R, Moiseev A, Vrba J, Murphy P, Preissl H and Eswaran H 2006 Optimal reduction of MCG in fetal MEG recordings *IEEE Trans. Biomed. Eng.* **53** 1720–4

Mescher M J, Lutwak R and Varghese M 2005 An ultra-low-power physics package for a chip-scale atomic clock *13th International Conference on Solid-State Sensors, Actuators and Microsystems* **1** 311–6

Mhaskar R, Knappe S and Kitching J 2012 A low-power, high-sensitivity micromachined optical magnetometer *Appl. Phys. Lett.* **101** 241105–4

Oostendorp T F, Van Oosterom A and Jongsma H W 1989a The effect of changes in the conductive medium on the fetal ECG throughout gestation *Clin. Phys. Physiol. Meas.* **10** 11–20 (suppl. B)

Oostendorp T F, Van Oosterom A and Jongsma H W 1989b Electrical properties of tissues involved in the conduction of foetal ECG *Med. Biol. Eng. Comput.* **27** 322–4

Pieri J F, Crowe J A, Hayes-Gill B R, Spencer C J, Bhogal K and James D K 2001 Compact long-term recorder for the transabdominal foetal and maternal electrocardiogram *Med. Biol. Eng. Comput.* **39** 118–25

Quinn A, Weir A, Shahani U, Bain R, Maas P and Donaldson G 1994 Antenatal fetal magnetocardiography: a new method for fetal surveillance? *Br. J. Obstet. Gynaecol.* **101** 866–70

Sameni R and Clifford G D 2010 A review of fetal ECG signal processing; issues and promising directions *Open Pacing Electrophysiol. Ther. J.* **3** 4–20

Sander T H, Burghoff M, Van Leeuwen P and Trahms L 2007 Application of decorrelation-independent component analysis to biomagnetic multi-channel measurements *Biomed. Tech.* **52** 130–6

Sander T H, Preusser J, Mhaskar R, Kitching J, Trahms L and Knappe S 2012 Magnetoencephalography with a chip-scale atomic magnetometer *Biomed. Opt. Express* **3** 981–90

Scofield J H 1994 Frequency-domain description of a lock-in amplifier *Am. J. Phys.* **62** 129–133

Shah V K and Wakai R T 2013 A compact, high performance atomic magnetometer for biomedical applications *Phys. Med. Biol.* **58** 8153

Steinhoff U, Link A, Wiekhorst F, Bader M, Knappe-Graeneberg S and Ackermann R 2005 Complex narrow band-pass filters for QRS detection in contactless magnetocardiograms of small animals *Comput. Cardiol.* **32** 467–70

Strasburger J F, Cheulkar B and Wakai R T 2008 Magnetocardiography for fetal arrhythmias *Heart Rhythm* **5** 1073–6

Strasburger J F and Wakai R T 2010 Fetal cardiac arrhythmia detection and *in utero* therapy *Nat. Rev. Cardiol.* **7** 277–90

Van Leeuwen P, Lange S, Klein A, Geue D, Zhang Y, Krause H J and Gronemeyer D 2004 Reproducibility and reliability of fetal cardiac time intervals using magnetocardiography *Physiol. Meas.* **25** 539–52

Van Leeuwen P, Werner L, Hilal Z, Schiermeier S, Hatzmann W and Gronemeyer D 2014 Fetal electrocardiographic measurements in the assessment of fetal heart rate variability in the antepartum period *Physiol. Meas.* **35** 441–54

Vrba J, Robinson S E, Mccubbin J, Lowery C L, Eswaran H, Wilson J D, Murphy P and Preissl H 2004 Fetal MEG redistribution by projection operators *IEEE Trans. Biomed. Eng.* **51** 1207–18

Vullings R and Mischi M 2013 Probabilistic source separation for robust fetal electrocardiography *Comput. Math. Methods Med*. **2013** 109756

Wakai R T, Lengle J M and Leuthold A C 2000 Transmission of electric and magnetic foetal cardiac signals in a case of ectopia cordis: the dominant role of the *vernix caseosa Phys. Med. Biol.* **45** 1989–95

Wilson J D, Govindan R B, Hatton J O, Lowery C L and Preissl H 2008 Integrated approach for fetal QRS detection *IEEE Trans. Biomed. Eng.* **55** 2190–7

Wyllie R, Kauer M, Wakai R T and Walker T G 2012 Optical magnetometer array for fetal magnetocardiography *Opt. Lett.* **37** 2247–9

Xia H, Baranga A B-A, Hoffman D and Romalis M V 2006 Magnetoencephalography with an atomic magnetometer *Appl. Phys. Lett.* **89** 211104–3

Ziehe A and Müller K-R 1998 TDSEP—an efficient algorithm for blind separation using time structure *ICANN 98* ed L Niklasson *et al* (London: Springer) pp 675–80